Supplementary material

Nanoscale Phase Measurement for the Shale Challenge: Multi-component Fluids in Multi-scale Volumes

Junjie Zhong[†], Yinuo Zhao[‡], Chang Lu[‡], Yi Xu[†], Zhehui Jin[‡], Farshid Mostowfi[§] and David Sinton[*, †]

[†] Department of Mechanical and Industrial Engineering, University of Toronto, 5 King's College Road, Ontario, Toronto M5S 3G8, Canada

[‡] Department of Civil and Environmental Engineering, University of Alberta, 9211 - 116 Street NW, Edmonton, Alberta T6G 1H9, Canada

[§] Schlumberger-Doll Research, 1 Hampshire Street, Cambridge, Cambridge, Massachusetts 02139, USA

[*] corresponding author: sinton@mie.utoronto.ca

Contents

Section 1: Nanofluidic chip fabrication

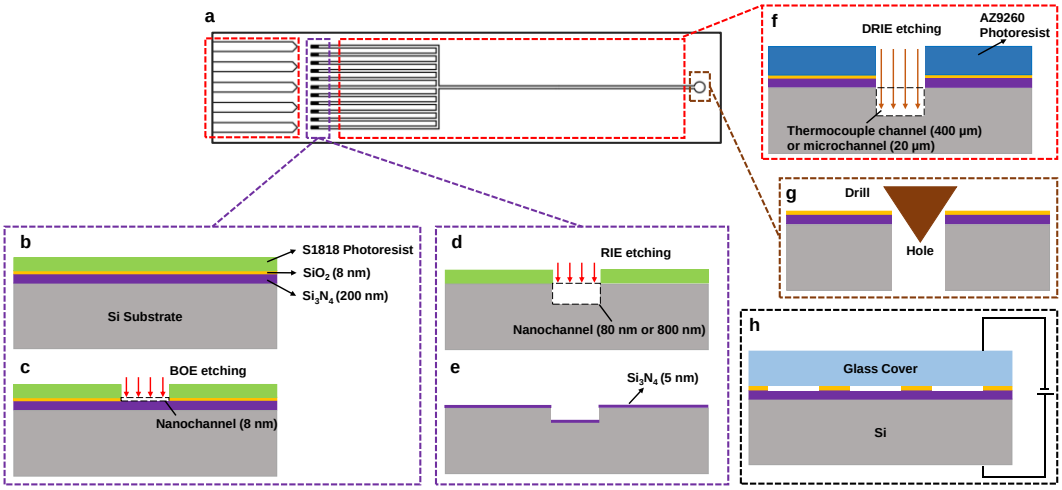

Figure S1. Chip fabrication procedures. (a) Schematic of the nanofluidic chip design. (b) 8-nm deep nanochannel fabrication: silicon substrate with a 200 nm silicon nitride layer deposited through LPCVD, a 8-nm silicon dioxide layer deposited through PECVD and a S1818 photoresist spin-coated layer. (c) 8-nm deep nanochannels etched through BOE (10:1) after removing photoresist from the exposure area. (d) 80-nm and 800-nm deep nanochannels fabrication: nanochannel directly etched by RIE on a silicon substrate are 80 nm and 800 nm after removal of photoresist from the exposure area. (e) Depositing a 5-nm thick silicon nitride layer on the nanochannel surface to have the same surface condition as the 8-nm channel case. (f) DRIE etching for reservoir and thermocouple microchannels. (g) Inlet hole drilled for the reservoir channel. (h) Anodic bonding of the chip after using Piranha solution (H_2SO_4:H_2O_2 = 3:1).

The nanofluidic chip used in this study was fabricated on the silicon wafer (chip design is shown in Figure S1a). To fabricate 8-nm deep nanochannels, a 200-nm silicon nitride film and an 8-nm silicon dioxide film were first deposited onto the substrate silicon wafer through low pressure chemical vapor deposition (LPCVD, Expertech CTR-200 LPCVD) and plasma-enhanced chemical vapor deposition (PECVD, Oxford Instruments PlasmaLab System 100 PECVD), followed by spin coating of S1818 photoresist, as shown in Figure S1b. The channel pattern was generated on the S1818 photoresist through standard photolithography, as shown in Figure S1c. After etching through buffered oxide etch (10:1) for 30 s, the 8-nm deep nanochannel was obtained. 80-nm

and 800-nm deep channels were fabricated using a dry etching method instead (through reactive ion etching, RIE, Oxford PlasmaPro 100 Cobra ICP-RIE, Figure S1d). To keep the same nanochannel surface condition as the 8-nm deep channel case, a 5-nm silicon nitride layer was deposited on the etched chip via LPCVD (Figure S1e).

After nanochannels were fabricated, the S1818 photoresist was cleaned with a Piranha solution (H_2SO_4:H_2O_2 = 3:1) for 20 min. AZ9260 photoresist was then spin-coated on the wafer to fabricate deep microchannels and thermocouple channels. To etch the microchannels and thermocouple channels on the wafer (Figure S1f), we applied deep reactive ion etching (DRIE, Oxford Instruments PlasmaPro Estrelas100 DRIE System). Afterwards, inlet holes were drilled on the silicon substrate at the inlet of the microchannel, as shown in Figure S1g. The silicon wafer and a piece of 2.2 mm-thick borosilicate glass were then cleaned in Piranha solution (H_2SO_4:H_2O_2 = 3:1) for another 20 min, and bonded together through anodic bonding (AML AWB-04 Aligner Wafer Bonder) to seal channels, as shown in Figure S1h. Bonding the 8-nm nanofluidic chip was at 673.15 K and at vacuum, with a voltage of 100 V for 2 min (charge reaching ~100 mC). The highest fluid pressure tested within the 8-nm chip was 5 MPa. Bonding 80-nm and 800-nm nanofluidic chips was performed at 673.15 K and vacuum, with a voltage at 600 V for 10 min (charge reaching ~1000 mC). The highest tested fluid pressure within the 80-nm and 800-nm chip was 12 MPa. Lastly, the chip was cut into the designed shape with a dicing machine (Disco DAD3220 Automatic Dicing Saw).

Section 2: Experimental setup and procedures for mixture dew point and bubble point measurement

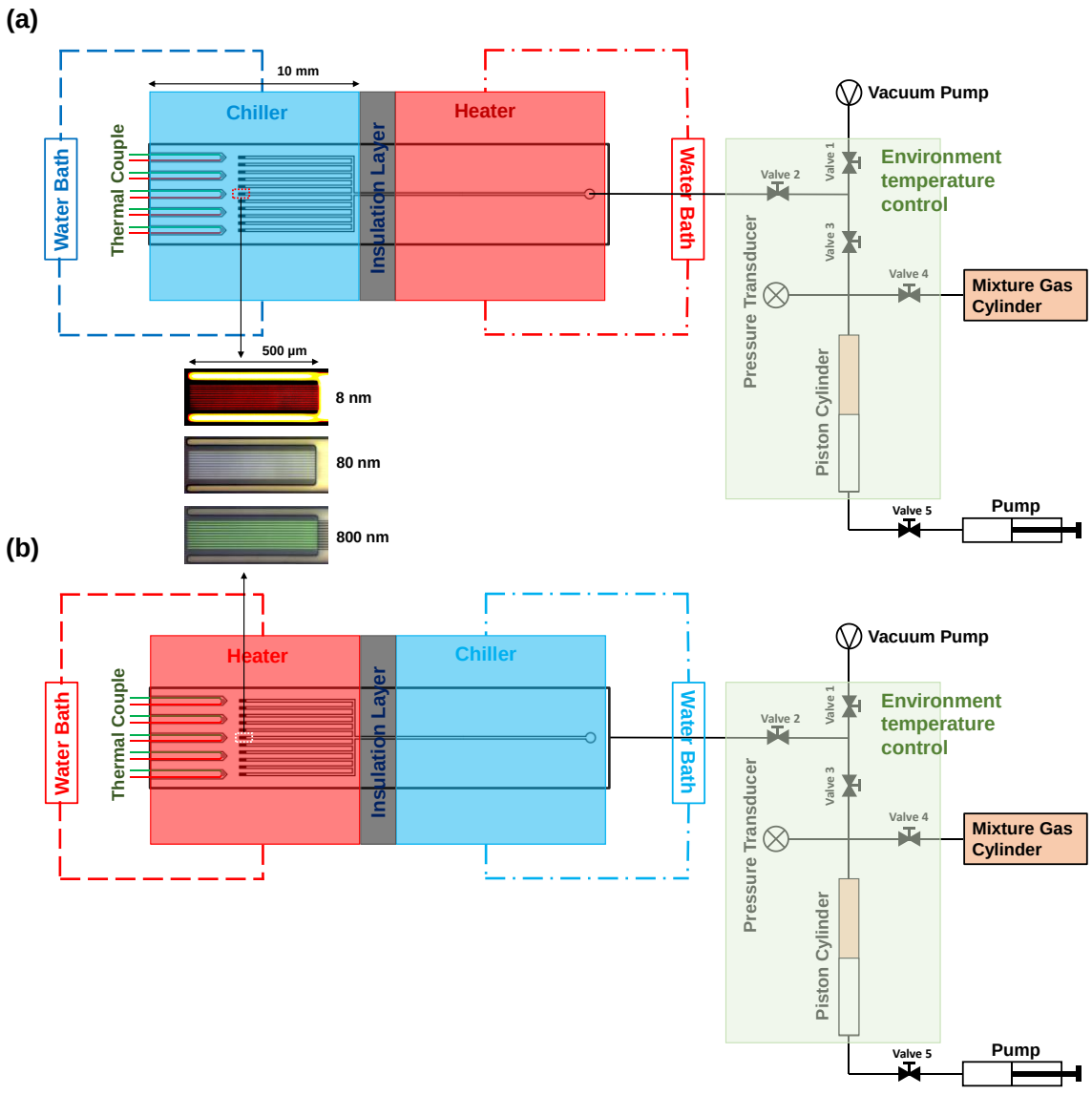

Figure S2. Diagram of the experimental setup. Nanofluidic chip mounted on a manifold capable of connecting the chip to pipelines, where the methane/propane mixture pressure was closely controlled through the pump and piston cylinder. A temperature gradient on the chip was introduced through the copper heater/chiller, controlled by water baths, and monitored by thermocouples inserted into the chip close to the nanochannel. The environmental temperature was also closely controlled during the experiments. To study the mixture dew point, the temperature around nanochannels was set as the

lowest within the entire system, (a). To study the mixture bubble point, the temperature around nannochannels was set as the highest within the entire system, (b).

The experimental system is shown in Figure S2. The chip and manifold were connected to a methane/propane mixture gas cylinder (20% mole concentration methane balanced by propane, Praxair Canada Inc., purity > 99.99%), syringe pump (TELEDYNE ISCO MODEL 260D, resolution at 0.001 MPa), and piston cylinder (HIP 70C3-10-P). At first use, the entire system was vacuumed at 2 x 10^{-7} MPa (PFPE RV8) for 3 hrs at room temperature (293.15 K), ensuring the impurity introduced by air is <0.01%, followed by isolation for another 3 hrs to perform a leak test. The temperature gradient was introduced and controlled by two water baths (Cole-Parmer Polystat® Standard 6.5L Heated Bath, error is ± 0.01 K), through two copper blocks (10 mm along the channel direction and 50 mm perpendicular to the channel direction) clamped on the silicon side of the chip, namely chiller and heater. The chiller and heater positions could be changed based on the nature of tests performed (i.e., dew point test or bubble point test), and were separated by a thick insulation layer (Alumina Oxide Fiber, ~1 mm thick). The region of interest (500 µm long nanochannels) was designed to be covered by the center of the chiller/heater as specified in Figure S2, in which the nanochannels were ensured to be tested under isothermal conditions. During the test, the system pressure was monitored by the pressure transducer (PX409-3.5KGUSBH). Mixture phase behavior was captured directly and observed in real-time using a camera (Leica DMC 2900, recording at 5 frames per second) connected to the optical microscope (Leica DM 2700M). The spatial resolution for the image was 0.3 µm/pixel. The experimental setup described here is similar to the experimental setup used in our previous work on pure hydrocarbon condensation[1].

To study the dew point of the mixture, the temperature gradient was first applied on the chip through two water baths. The temperature of the environment, inlet of the chip as well as the microchannel region were maintained at 300.15 K, and the region containing the dead-end nanochannels was set to temperatures from 282.15 to 300.15 K (3 K as the interval). Under these conditions, the condensation was forced to initiate from the dead-end region when the system is pressurized (initially a pure vapor phase). The fluidic network was first vacuumed for three

hours, and loaded with premixed methane/propane mixture (1 : 4 mole ratio) at 0.55 MPa and 300.15 K as gas. At isothermal condition, the entire system was pressurized stepwise (0.01 MPa) with a syringe pump. Diffusion in the 500 μm long nanochannel requires ~3 min to reach equilibrium (<0.01% difference of composition, Figure S3 (d)). The pressure of the initiation of condensation in nanochannels was detected in real-time via an optical microscope and a pressure transducer monitoring the entire system.

To perform the pressure drawdown for studying the mixture bubble point, similarly a temperature gradient was firstly introduced across the chip. In this case the setup environment, inlet of the chip as well as the microchannel region were maintained at 278.15 K, and the dead-end region was set at 288.15 K. The cavitation was thus forced to initiate at the dead-end region when the system was depressurized from a pure liquid phase. After vacuuming the system and filling the system with a gas mixture, the entire system was pressurized to 4.5 MPa at isothermal conditions, and the mixture was in liquid phase.

The first pressure drawdown test was in the equilibrium condition as a control group, where the system pressure was reduced stepwise (0.05 MPa) with a 15 min waiting time at each step. The results are recorded for later comparison. Then, continuously pressure drawdown was performed by mixture volume expansion at a constant rate provided by the syringe pump. The slow expansion rate (50 μL/min) and fast expansion rate (50 ml/min) led to different pressure drawdown curves as shown in Figure S3. During the slow expansion, the mixture vaporization dynamics and the initiation of vaporization were very close to that detected in the equilibrium pressure drawdown. This similarity explains how such a slow pressure drawdown rate allowed the system to reach pressure and chemical potential equilibrium everywhere at any given moment (estimated in Section 3). Therefore, this test could be considered a near-equilibrium pressure drawdown case. In the fast expansion case, however, the rate of pressure change was much greater than that estimated by the diffusion rate (Section 3). The results here were very different from the results of the equilibrium pressure drawdown, and thus this test can be considered as an example of non-equilibrium pressure drawdown.

Section 3: Near-equilibrium pressure drawdown and non-equilibrium pressure drawdown

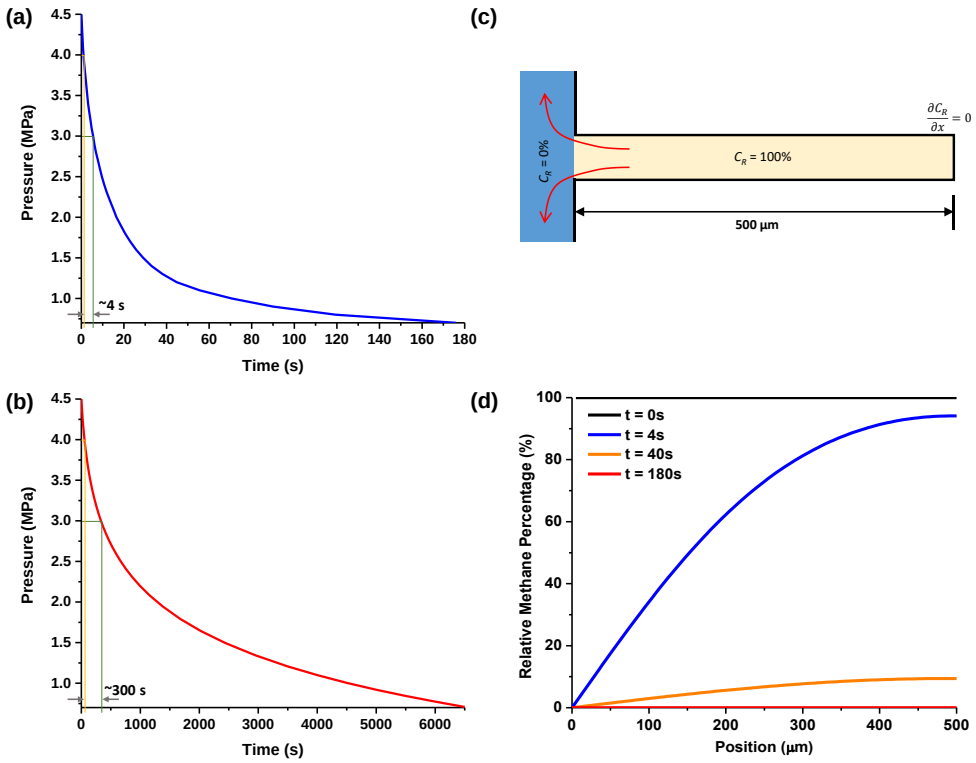

Figure S3. System pressure drawdown history (from 4.5 MPa to 0.7 MPa) of the (a) non-equilibrium and (b) near-equilibrium pressure drawdown test at 288.15 K. (c) An extreme initial and boundary condition for considering building chemical potential equilibrium in the system, where methane in the 500-μm long nanochannel (initial methane relative concentration is 100%) diffuses to the microchannel (0% and constant). (d) Relative methane concentration profile in nanochannel calculated at 0s, 4s, 40s and 180s.

During the mixture bubble point test, the system pressure reduction history was closely monitored through a pressure transducer, as shown in Figure S3a and b for the non-equilibrium and near-equilibrium pressure drawdown, respectively. Vaporization in the experimental system is highly likely to happen close to the theoretical mixture bubble point in bulk (3.77 MPa), here defined as a range from 3.0 - 4.0 MPa. The time taken for the system pressure to pass this range for the non-equilibrium case was ~4s (Figure S3a), and for the near-equilibrium this time was ~300s (Figure S3b). As for the non-equilibrium case, the concentration of methane in the whole system during such a short time period (4s) is potentially not able to reach equilibrium. This effect

can be estimated through a 1-D diffusion model by considering an extreme initial and boundary condition, where methane in the 500-μm long nanochannel has an initial relative concentration of 100%, and in the microchannel has an initial relative concentration of 0% (fixed, as the microchannel has a significantly larger volume than the nanochannel. In this case, the diffusivity of methane is calculated via the Stokes–Einstein equation to be 6.5×10^{-9} m^2/s (methane molecule is 0.4 nm, liquid mixture viscosity at 288.15 K is 81 μPa.s). Solving the diffusion equation numerically under these conditions at 40s shows that the average concentration of methane in the nanochannel has been reduced to only ~5% of its original concentration, thus ~95% methane in the nanochannel has diffused to the microchannel and the whole system is very close to equilibrium (Figure S3d). At 4s, the average methane concentration in the nanochannel is ~70% of its original concentration, which is far away from equilibrium. Therefore, for the non-equilibrium pressure drawdown test, system chemical potential (i.e., methane concentration) equilibrium was not reached, as it was limited by the slow diffusion process compared to the fast pressure drawdown rate.

Section 4: Peng-Robinson equation of state (PR-EOS) with capillary pressure model

In this work, we use the PR-EOS with a capillary pressure model and set a constant volume, temperature and number of moles of hydrocarbon species, namely VT-Flash. VT-Flash with capillary pressure is used to calculate the lower dew point of C_1-C_3 (methane - propane) mixtures under confinement. Considering the effect of capillary pressure P_{ca} and assuming that the liquid phase wets the pore surfaces, the phase equilibrium is obtained by satisfying two conditions[2]:

$$P^V\left(V^V, T, n_{C_1}^V, n_{C_3}^V\right) - P^L\left(V^L, T, n_{C_1}^L, n_{C_3}^L\right) = P_{ca} \tag{1}$$

and

$$\mu_i^V\left(V^V, T, n_{C_1}^V, n_{C_3}^V\right) = \mu_i^L\left(V^L, T, n_{C_1}^L, n_{C_3}^L\right) \quad i = C_1, C_3 \tag{2}$$

in which, T is the system temperature; V^V and V^L represent the vapor and liquid phase volumes, respectively; P^V and P^L depict the vapor and liquid phase pressures, respectively; μ_i^V and μ_i^L represent the chemical potentials of C_1 and C_3 in the vapor phase and liquid phase, respectively; $n_{C_1}^L$ and $n_{C_3}^L$ depict the mole numbers of C_1 and C_3 in liquid phase, respectively; $n_{C_1}^V$ and $n_{C_3}^V$ represent the mole numbers of C_1 and C_3 in vapor phase, respectively.

We assume that hydrocarbon mixtures are confined by two infinitely large planar slits separated by a distance W. Thus, based the Young-Laplace equation[3] with zero contact angle, the capillary pressure can be calculated as:

$$P_{ca} = \frac{2\sigma}{W}\ , \tag{3}$$

where σ is the vapor-liquid interfacial tension (IFT). The IFT can be obtained by Parachor model[4]:

$$\sigma = \left[\sum_{i=C_1,C_3} \chi_i \left(x_i \rho_m^L - y_i \rho_m^V \right) \right]^4 \tag{4}$$

in which χ is the Parachor number, ρ_m^L and ρ_m^V are the mole density of the liquid phase and vapor phase, respectively; x_i and y_i are the mole fractions of component i in the liquid phase and vapor phase, respectively.

To solve the chemical potential equilibrium Eq. (2), Mikyška and Firoozabadi[5] proposed a modeling framework based on the volume function rather than fugacity. The Volume function is defined as an effective partial volume of a real fluid. Similarly, a dimensionless parameter volume function coefficient Φ is proposed to relate the ideal fluid volume to volume function, which plays an analogous role to the fugacity coefficient in constant pressure and temperature (PT)-Flash. In terms of volume function coefficient Φ_i^V and Φ_i^L, Eq. (2) can be expressed as[5]:

$$\frac{n_i^V}{V^V \Phi_i{}^V \left(V^V, T, n_{C_1}^V, n_{C_3}^V \right)} = \frac{n_i^L}{V^L \Phi_i{}^L \left(V^L, T, n_{C_1}^L, n_{C_3}^L \right)}, \quad i = C_1, C_3 \ . \tag{5}$$

In this work, the volume function coefficient is obtained from the PR-EOS, which is given as[6]:

$$P\left(V, T, n_{C_1}, n_{C_3}\right) = \frac{nRT}{V - B} - \frac{A}{V^2 + 2BV - B^2} \ . \tag{6}$$

where R is the universal gas constant, n is the total number of moles. The coefficients A and B are given as

$$A = \sum_{i=C_1,C_3} \sum_{j=C_1,C_3} n_i n_j a_{ij} \tag{7a}$$

$$a_{ij} = (1 - k_{ij}) \sqrt{a_i a_j} \tag{7b}$$

$$B = \sum_{i=C_1,C_3} n_i b_i \tag{7c}$$

in which, a_i is the attraction parameter and b_i is the repulsion parameter for component i, respectively; k_{ij} is the binary interaction parameter (BIP) between the component i and j. BIP is selected to match the lower dew point and bubble point of C_1-C_3 mixtures from PR-EOS with experiments. a_i and b_i are given by

$$a_i = 0.45724 \frac{R^2 T_{i,c}^2}{P_{i,c}} \left[1 + m_i (1 - \sqrt{T_{r,i}}) \right]^2 \tag{8a}$$

$$b_i = 0.0778 \frac{R T_{i,c}}{P_{i,c}} \tag{8b}$$

and

$$T_{r,i} = \frac{T}{T_{i,c}} \tag{9}$$

$$m_i = \begin{cases} 0.37464 + 1.54226\omega_i - 0.26992\omega_i^2 & \omega_i < 0.5, \\ 0.3796 + 1.485\omega_i - 0.1644\omega_i^2 + 0.01667\omega_i^3 & \omega_i \geq 0.5, \end{cases} \tag{10}$$

where $T_{i,c}, P_{i,c}, \text{and } \omega_i$ are critical temperature, critical pressure and acentric factor of component i, respectively. The volume function coefficient for the PR-EOS is given as[6]:

$$\ln \Phi_i = \ln \frac{V - B}{V} - \frac{b_i n}{V - B} + \frac{A b_i}{BRT} \frac{V}{V^2 - 2BV - B^2} - \frac{1}{\sqrt{2} BRT} \left[\frac{A b_i}{2B} - \sum_{j=1}^{m} n_j a_{ij} \right] \ln \left| \frac{V + (1 + \sqrt{2})B}{V + (1 - \sqrt{2})B} \right| \tag{11}$$

An iterative method is used to track the lower dew point by VT-Flash with a capillary pressure algorithm. In the inner loop, the interior point method is used to solve the vapor-phase fraction. In the outer loop, the volume fraction of the vapor phase is updated by solving Eq. (1), and then the equilibrium ratio K is updated by solving the chemical potential equilibrium equation. We continue the iterations until the variation is less than a tolerance parameter. At lower dew point, for vapor-liquid two phase coexistence, the vapor phase fraction is close to 1, while the liquid phase fraction is negligible. The related parameters are presented in Table S1.

Table S1: PR-EOS parameters for C_1 and C_3

Component	T_c (K)	P_c (bar)	ω	Mw (g/mol)	χ	BIP
C_1	190.56	45.99	0.011	16.04	77.33	0.006
C_3	369.83	42.48	0.153	44.1	157.31	

Section 5: Engineering density functional theory

Within the framework of engineering density functional theory (DFT), the hydrocarbon fluids confined nanopores are in chemical equilibrium with "an infinite fictitious bulk reservoir", i.e., chemical potentials of hydrocarbon fluids in nanopores are the same as that in bulk. In this work, the nanochannels are connected with microchannels, allowing energy and mass exchange between them. Compared to the volume of microchannels, the volume of nanochannels is negligible. Thus, competitive adsorption in nanochannels does not affect hydrocarbon fluids in microchannels which can serve as the "fictitious bulk reservoir".

Within the framework of DFT, the equilibrium properties are obtained by the minimization of the grand potential functional $\Omega\left[\{\rho_i(\mathbf{r})\}\right]$ which is the functional of density distribution $\{\rho_i(\mathbf{r})\}$ and related to the Helmholtz free energy functional $F\left[\{\rho_i(\mathbf{r})\}\right]$[7],

$$\Omega\left[\{\rho_i(\mathbf{r})\}\right] = F\left[\{\rho_i(\mathbf{r})\}\right] + \sum_i \int \rho_i(\mathbf{r})\left[\Psi_i(\mathbf{r}) - \mu_i\right] d\mathbf{r}, \tag{15}$$

where $d\mathbf{r}$ is the differential volume, and $\rho_i(\mathbf{r})$ is the number density distribution of component i at position $\mathbf{r}$; $\varphi_i(\mathbf{r})$ represents the external potential exerted on the component i at the position $\mathbf{r}$; μ_i is the chemical potential of component i. When the system pressure is above P_{bub}^{bulk} or lower than P_{dew}^{bulk}, the bulk fluids are in a single phase. We use the chemical potentials of C_1 and C_3 in single phase for the DFT calculation. However, when the system pressure is between P_{bub}^{bulk} and P_{dew}^{bulk}, the bulk hydrocarbon fluids are in vapor-liquid coexistence with equivalence of chemical potentials in two phases. Thus, we use chemical potentials of C_1 and C_3 in liquid phase

for DFT calculation. The chemical potentials of fluids in engineering DFT are obtained from PR-EOS[6].

At equilibrium, the grand potential functional is at a minimum,

$$\frac{\delta\Omega\left[\left\{\rho_i\left(\mathbf{r}\right)\right\}\right]}{\delta\rho_i\left(\mathbf{r}\right)}=0\,. \tag{16}$$

In Eq. (16), the symbol δ represents the functional derivative. With an appropriate expression for the excess Helmholtz free energy functional $F^{ex}\left[\left\{\rho_i\left(\mathbf{r}\right)\right\}\right]$, minimization of the grand potential functional yields the Euler-Lagrange equation[7],

$$\rho_i\left(\mathbf{r}\right)=\exp\left[\beta\mu_i-\beta\varphi_i\left(\mathbf{r}\right)-\delta\beta F^{ex}\left[\left\{\rho_i\left(\mathbf{r}\right)\right\}\right]/\delta\rho_i\left(\mathbf{r}\right)\right], \tag{17}$$

where $\beta=1/\left(k_BT\right)$, k_B is the Boltzmann constant and T is the absolute temperature. In our engineering DFT, the excess Helmholtz free energy functional is divided into two parts: one part is obtained from the PR-EOS[6, 8] by adopting the WDA[9] to account for physical interactions between fluid molecules; the other part is supplemented by the quadratic density expansion to account for long-range interactions[10-11] which vanishes in the bulk. The critical properties, acentric factors, molecular weight, and BIP for engineering DFT are the same as that used in PR-EOS with the capillary pressure model as shown in Table S1. The attraction energy parameters ε_g for C_1 and C_3 in the quadratic density expansion for long-range interactions[12] in the engineering DFT are 1178 K and 1866 K, respectively. Details about engineering DFT can be referred to Li and Firoozabadi[12].

For simplicity, we use the structureless carbon to simulate the effect of nano-confinement and the fluid-surface interaction φ_{wf} is given by the 10-4-3 Steele potentials[13],

$$\varphi_{wf}\left(z\right)=2\pi\rho_w\varepsilon_{wf}\sigma_{wf}^2\Delta\left[\frac{2}{5}\left(\frac{\sigma_{wf}}{z}\right)^{10}-\left(\frac{\sigma_{wf}}{z}\right)^4-\frac{\sigma_{wf}^4}{3\Delta\left(0.61\Delta+z\right)^3}\right], \tag{18}$$

where $\rho_w = 114$ nm^{-3}, $\varepsilon_w = 28$ K, $\sigma_w = 0.3345$ nm, and $\Delta = 0.335$ nm, respectively. The Lorentz-Berthelot rules are used to obtain ε_{wf} and σ_{wf},

$$\varepsilon_{wf} = \sqrt{\varepsilon_w \varepsilon_f}\,, \tag{19}$$

$$\sigma_{wf} = \frac{1}{2}\left(\sigma_w + \sigma_f\right), \tag{20}$$

in which, ε_f and σ_f are energy and size parameter for the fluids. Similar to our previous work[14], the external potentials for C_1 and C_3 are modeled as one CH_4-wall interaction and the sum of two CH_3-wall and one CH_2-wall interactions, respectively. The parameters ε_f and σ_f are 129.63 K and 0.3679 nm for the methyl group (-CH_3), 73.5 K and 0.4 nm for the methylene group (-CH_2-), and 160.3 K and 0.373 nm for CH_4[15]. Although the experiment is conducted on silica-based materials, the phase behavior of hydrocarbon mixtures is dominated by the Van der Waals interactions, which are the governing forces in carbon-based materials. Thus, the behaviors of nano-confined hydrocarbon mixtures should be qualitatively the same.

The external potential Ψ in a slit pore is expressed as

$$\Psi(z) = \varphi_{wf}(z) + \varphi_{wf}(W - z), \tag{21}$$

where W is the slit-pore size. In a slit pore, the density distributions only vary in the z direction perpendicular to the solid surfaces, i.e., $\rho_i(\mathbf{r}) = \rho_i(z)$.

The average density of component i in nanopores $\rho_{ave,i}$ is given as,

$$\rho_{ave,i} = \frac{\int_0^W \rho_i(z)\,dz}{W}. \tag{22}$$

At isothermal condition, the bubble point of confined hydrocarbon mixtures is identified as the point of the equilibrium transition as reported in the previous work[16]. The equilibrium transition occurs at a point where condensation and desorption branches have the same grand potential calculated from Eq. (15). The condensation/desorption branches are obtained by gradually

increasing/decreasing system pressure while using fluid configurations in nanopores at the previous pressure condition as the initial condition. We use a successive substitution iteration[17] to update the density distributions by using the output of Eq. (17) as a new input. At the first pressure where the initial guess is not available, the bulk density is used for the initialization.

Reference

1. Zhong, J.; Riordon, J.; Zandavi, S. H.; Xu, Y.; Persad, A. H.; Mostowfi, F.; Sinton, D. Capillary Condensation in 8-nm Deep Channels. *J. Phys. Chem. Lett.* **2018,** *9*, 497-503.
2. Kou, J.; Sun, S. A stable algorithm for calculating phase equilibria with capillarity at specified moles, volume and temperature using a dynamic model. *Fluid Phase Equilib.* **2018,** *456*, 7-24.
3. Nojabaei, B.; Johns, R. T.; Chu, L. Effect of Capillary Pressure on Phase Behavior in Tight Rocks and Shales. *SPE Reservoir Eval. Eng* **2013,** *16*, 281-289.
4. Weinaug, C. F.; Katz, D. L. Surface Tensions of Methane-Propane Mixtures. *Ind. Eng. Chem.* **1943,** *35*, 239-246.
5. Mikyška, J.; Firoozabadi, A. A new thermodynamic function for phase-splitting at constant temperature, moles, and volume. *AIChE J.* **2011,** *57*, 1897-1904.
6. Peng, D.-Y.; Robinson, D. B. A New Two-Constant Equation of State. *Ind. Eng. Chem. Fundam.* **1976,** *15*, 59-64.
7. Evans, R. The nature of the liquid-vapour interface and other topics in the statistical mechanics of non-uniform, classical fluids. *Adv. Phys.* **1979,** *28*, 143-200.
8. Robinson, D. B.; Peng, D.-Y.; Chung, S. Y. K. The development of the Peng - Robinson equation and its application to phase equilibrium in a system containing methanol. *Fluid Phase Equilib.* **1985,** *24*, 25-41.
9. Rosenfeld, Y. Free-energy model for the inhomogeneous hard-sphere fluid mixture and density-functional theory of freezing. *Phys. Rev. Lett.* **1989,** *63*, 980-983.
10. Ebner, C.; Saam, W. F. New Phase-Transition Phenomena in Thin Argon Films. *Phys. Rev. Lett.* **1977,** *38*, 1486-1489.
11. Ebner, C.; Saam, W. F.; Stroud, D. Density-functional theory of simple classical fluids. I. Surfaces. *Phys. Rev. A* **1976,** *14*, 2264-2273.
12. Li, Z.; Firoozabadi, A. Interfacial tension of nonassociating pure substances and binary mixtures by density functional theory combined with Peng–Robinson equation of state. *J. Chem. Phys.* **2009,** *130*, 154108.
13. Steele, W. A. The physical interaction of gases with crystalline solids: I. Gas-solid energies and properties of isolated adsorbed atoms. *Surf. Sci.* **1973,** *36*, 317-352.
14. Jin, Z. Bubble/dew point and hysteresis of hydrocarbons in nanopores from molecular perspective. *Fluid Phase Equilib.* **2018,** *458*, 177-185.
15. Errington, J. R.; Panagiotopoulos, A. Z. A New Intermolecular Potential Model for the n-Alkane Homologous Series. *J. Phys. Chem. B* **1999,** *103*, 6314-6322.
16. Ravikovitch, P. I.; Domhnaill, S. C. O.; Neimark, A. V.; Schueth, F.; Unger, K. K. Capillary Hysteresis in Nanopores: Theoretical and Experimental Studies of Nitrogen Adsorption on MCM-41. *Langmuir* **1995,** *11*, 4765-4772.
17. Li, Z.; Jin, Z.; Firoozabadi, A. Phase Behavior and Adsorption of Pure Substances and Mixtures and Characterization in Nanopore Structures by Density Functional Theory. *SPE J.* **2014,** *19*, 1096-1109.